Dynamic modelling of strainbursting around tunnels

A Rigby *Institute of Mine Seismology, Australia*

Abstract

Crush-type seismic sources locating to tunnels are abundant at many mines, particularly those where stress is high and the rock is competent. These events are associated with the dynamic stress fracturing of rock around a tunnel and the convergence of the surrounding elastic rock mass into the tunnel's void. When associated with observable damage to the excavation, such events are termed strainbursts. Given that strainbursts can pose significant risk both in terms of safety and impact on production, understanding the demand they place on the ground support system is a problem of practical interest.

The demand placed on support by a given strainburst depends on how failure in the rock develops dynamically in space and time. While some information about this failure can be inferred from seismic data, it cannot provide a full description on its own. To gain further insight, we have conducted dynamic three-dimensional modelling of strainbursting around a tunnel for various cases of loading conditions and rock mass properties.

The results of these cases are analysed to quantify aspects of the source dynamics. In particular, we estimate the velocities and durations of failure propagation axially along the tunnel and radially outwards from the tunnel's surface. It is shown that these velocities, particularly in the case of radial propagation, are significantly lower than that expected for confined shear failure. We have also determined moment tensors, which give information about static/permanent deformation at the source. For each of the modelled cases, the moment tensor was of crush-type with a P-axis approximately aligned with maximum in-plane loading of the tunnel.

Keywords: *strainbursting, numerical modelling, seismic sources*

1 Introduction

As proposed by Ryder (1988), seismic events in mines can be categorised into slip-type/shear-type and crush-type sources. At many mines, a large number of these crush-type events locate to tunnels, which correspond to episodes of dynamic stress fracturing and the associated convergence of the surrounding rock mass (Malovichko & Rigby 2022). When associated with observable damage to the excavation, such sources are termed strainbursts, which can pose a significant risk to safety and production.

An episode of strainbursting around a tunnel can be interpreted as a sudden increase in the depth of failure (Malovichko & Rigby 2022), as shown in Figure 1. Here, the existing volume of failed rock (shown in yellow) suddenly expands (shown in red). In isotropic conditions, this expansion is concentrated in the direction orthogonal to maximum in-plane loading, the amplitude of which is given by σ_{max}. In this direction, the tunnel's effective diameter grows from a pre-strainburst value of D by the depth of failure increase $\Sigma\Delta d_f = \Delta d_f{}^1 + \Delta d_f{}^2$ cumulated across both sides of the tunnel. If the strainburst extends along a segment of tunnel with length L_A and the average depth of failure increase across this segment is $\Sigma\Delta d_f$, then the source's scalar moment can be estimated as

$$|\mathbf{M}| = 2\frac{1-\nu}{1-2\nu}|\sigma_{max}|DL_A\overline{\sum\triangle d_f},$$

(1)

where ν is the Poisson's ratio of the rock mass (Malovichko & Rigby 2022).

By assuming a scaling relation between L_A and $\Sigma\Delta d_f$, it is therefore possible to estimate the depth of failure increase of a given strainburst from seismic data (Malovichko 2022). By further assuming a bulking factor,

this can be converted to an estimate of the displacement demand imposed on support by the strainburst (Kaiser & Malovichko 2022).
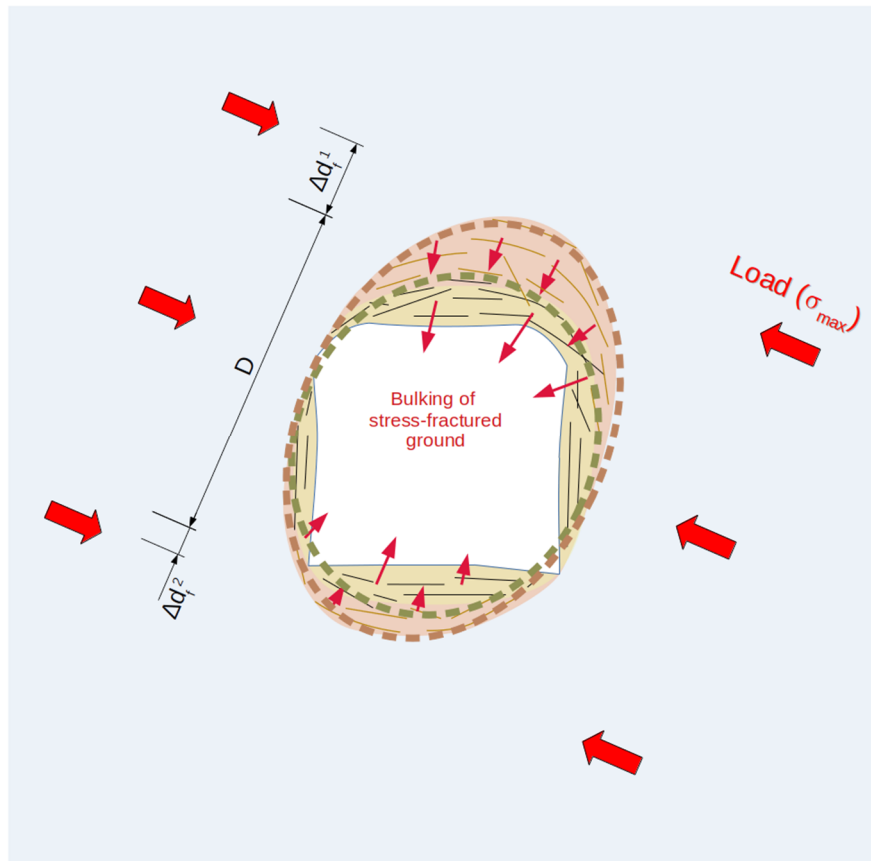

Figure 1 View looking along a tunnel showing failed rock before (yellow) and after (red) a strainburst. This increase in the damaged volume can be described in terms of an increase in the depth of failure as discussed in the main text

Assessing the energy demand imposed on support by a given strainburst also requires additional information about the dynamics of the source. In particular, an estimate must be made of the bulking duration. A procedure has been proposed for estimating the bulking time as twice the source's centroid time (Malovichko 2022), which can be inferred from seismic data. This is based on the seemingly reasonable assumption that source evolution is 'crack-like' in time, which is in keeping with the canonical model of Brune (1970) for slip-type/shear-type sources. However, the fact that energy demand is quite sensitive to the bulking duration estimate (there is an inverse-square relationship) motivates further investigation of source dynamics.

To gain further insight into these dynamics, we have conducted dynamic three-dimensional modelling of failure around a tunnel. This builds on previously published two-dimensional dynamic rockburst simulations (Malovichko & Rigby 2022; Manouchehrian & Cai 2018; Gao et al. 2019). Our modelling procedure is outlined in Section 2. This procedure has been followed for four cases of varying stress state and material properties, as described in Section 3. In Section 4, the results of these cases are analysed to estimate properties of the source dynamics, particularly the velocities and durations of failure propagation. In Section 5, we derive and analyse moment tensors for each case. The paper is concluded in Section 6.

2   Modelling procedure

2.1   Geometry

We considered an isolated 50 m section of horseshoe-shaped tunnel with a height and width of 5 m that is oriented north–south. We modelled this tunnel section and the surrounding rock mass using a tetrahedral mesh generated using TetGen (Hang 2015), as shown in Figure 2, which is composed of six regions:

- The red region (Region -1) corresponds to the interior of the tunnel and has a resolution of approximately 0.5 m.

- The green region (Region 1) extends to 2.5 m from the tunnel and is also regularly meshed at a resolution of approximately 0.5 m.

- The remaining regions (Regions 2–5) extend a further 25 m with a gradually increasing resolution up to approximately 3 m.

(a)   (b)
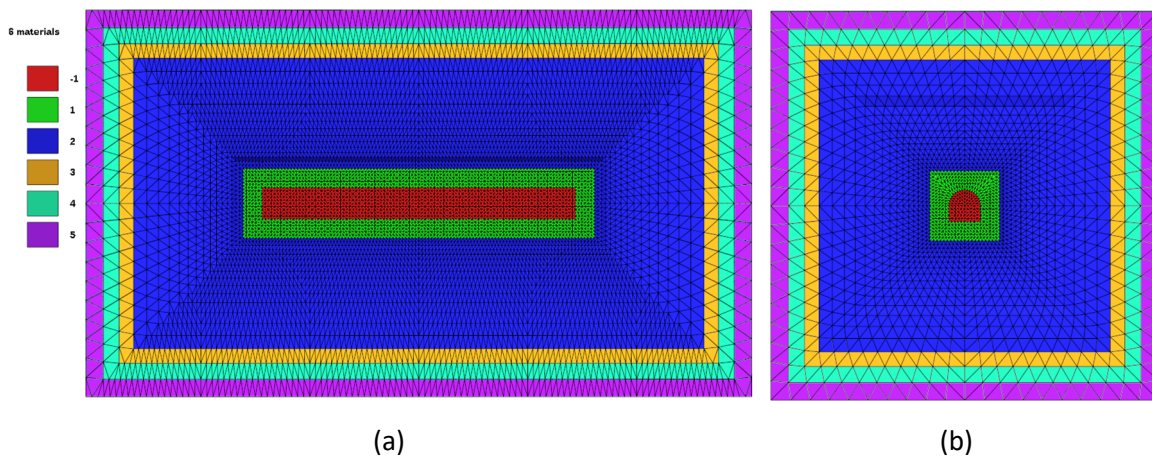
Figure 2   (a) Plan and (b) north views of the tetrahedral mesh describing the tunnel geometry and surrounding rock mass. The different regions are detailed in the main text

2.2   Material properties

We model the rock mass around the tunnel using a cohesion-weakening-friction-strengthening (CWFS) material (Diedrichs 2007; Hajiabdolmajid et al. 2002). Brittle failure at low confinement is implemented using an elastic-brittle-plastic constitutive relation with tension cutoff based on the formulation of Itasca Consulting Group (2009). Strain hardening at high confinement is implemented based on the strain softening constitutive model detailed by Sørensen et al. (2015). We note that the CWFS material model has been selected due to its simplicity and ability to reproduce relevant tunnel-scale behaviour.

The elastic parameters of the rock mass are fixed across the domain, with a Young's modulus of 75 GPa and Poisson's ratio of 0.25. At the midpoint of the tunnel, we use nominal parameters of friction angle ϕ = 25°, cohesion c = 50 MPa, residual friction angle ϕ_r = 50°, residual cohesion c_r = 2 MPa, dilation angle ψ = 20°, tensile strength σ_t = 16 MPa, and a deviatoric plastic strain limit $\varepsilon_c^p = \varepsilon_\phi^p$ = 3×10⁻³. To ensure that failure is localised near the middle of the tunnel section, we increase the nominal intact material parameters to values of ϕ = 50°, c = 100 MPa, and σ_t = 32 MPa at the ends of the tunnel. We consider cases where this increase is both symmetric and asymmetric. Taking y as position north from the tunnel's midpoint, the nominal cohesion for the symmetric case is:

$$c(y) = 50 \left[1 + \max(\frac{|y|}{25}, 1) \right] \text{ MPa,}$$

(2)

with ϕ and σ_t increasing in the same manner. For the asymmetric case, we instead take:

$$c(y) = 50 \left[1 + \begin{cases} \max(\frac{y}{5}, 1) & y > 0 \\ \max(\frac{-y}{25}, 1) & y \leq 0 \end{cases} \right] \text{MPa},$$

(3)

which means that strength increases more rapidly moving north from the tunnel's midpoint than moving south.

Beyond the variance in nominal parameters described above, we also randomly perturb both the intact and residual friction and cohesion using a Gaussian random field (note that dilation angle and deviatoric plastic strain limit are not perturbed). At a given point in space, the same multiplicative perturbation is applied to all parameters (ϕ, c, ϕ_r, c_r, and σ_t). These perturbations are obtained by generating uncorrelated Gaussian noise with a mean of 1 and standard deviation of 0.1, which is then convolved with a 5 m Gaussian kernel. We avoid unrealistic values by truncating the resulting field values within two standard deviations. Examples of the cohesion distribution following the application of this perturbation procedure are shown in Figure 3.
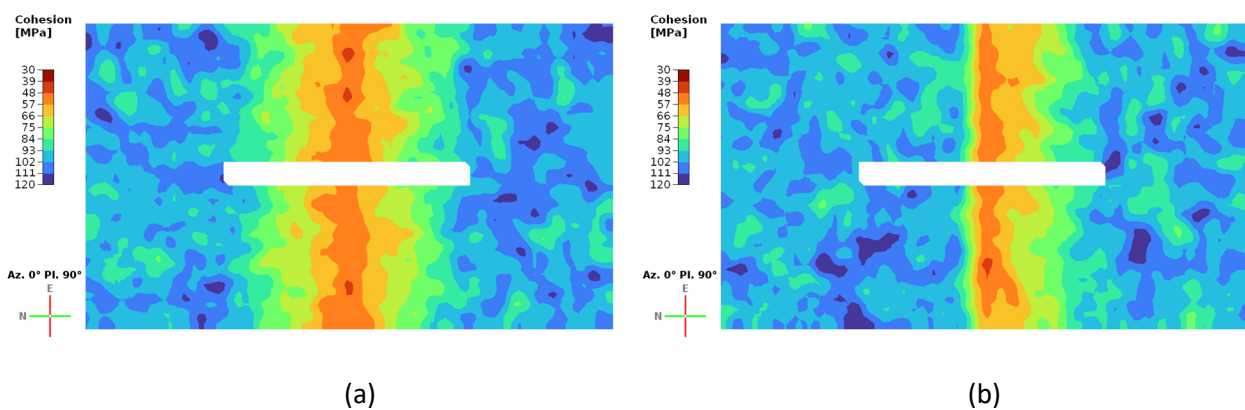

(a)   (b)

Figure 3   **(a) Plan view of example perturbed symmetric cohesion distribution on a horizontal plane intersecting the tunnel; (b) Same for asymmetric distribution**

2.3   Loading

We consider two different scenarios of the tunnel's loading. In the first scenario, we have σ_1 = 75 MPa oriented horizontally east–west (orthogonal to the tunnel's axis), σ_2 = 52.5 MPa oriented horizontally north–south (along the tunnel's axis), and σ_3 = 30 MPa oriented vertically. In the second scenario, the principal stress amplitudes remain unchanged, but the orientations of σ_1 and σ_3 are interchanged such that σ_1 is vertical.

2.4   Simulation

Simulation of a strainburst is conducted using the material point method (MPM) according to the following procedure:

- Each element of the tetrahedral grid outlined in Section 2.1 is populated with four particles (material points).

- Material properties are applied to each particle lying outside the tunnel, as described in Section 2.2. Particles inside the tunnel are assigned a very soft elastic material (E = 75 MPa and v = 0.25).

- A constant stress boundary condition is applied at the boundary of the domain. The same stress state is also applied to each particle (including those inside the tunnel) according to one of the loading scenarios outlined in Section 2.3.

- The pre-strainburst state is obtained by running the model to quasi-static equilibrium using damping, as described in Wang et al. (2016), with the elastic material inside the tunnel being slowly destressed over the first 100 iterations.

- To initiate the strainburst, the intact material parameters ϕ, c, and σ_t are instantaneously reduced by 10% for every particle outside of the tunnel.

- The post-strainburst state is obtained by running to equilibrium dynamically without damping in Regions -1, 1, and 2 of the tetrahedral mesh. Damping gradually increases across Regions 3, 4 and 5 to avoid reflections.

3 Cases

3.1 Case 1: horizontal loading, bidirectional failure

For the first case, maximum loading is horizontal (Section 2.3) and the material strength distribution is symmetric (Section 2.2). The evolution of failure as the strainburst progresses is shown in Figure 4 (note that we consider any particle that has accumulated plastic strain as having failed). Each row shows four views of the tunnel at a point in time with the failed volume of rock contoured in purple. It can be seen that failure is concentrated largely in the floor, beginning in the bottom western corner of the tunnel and propagating bidirectionally north and south.
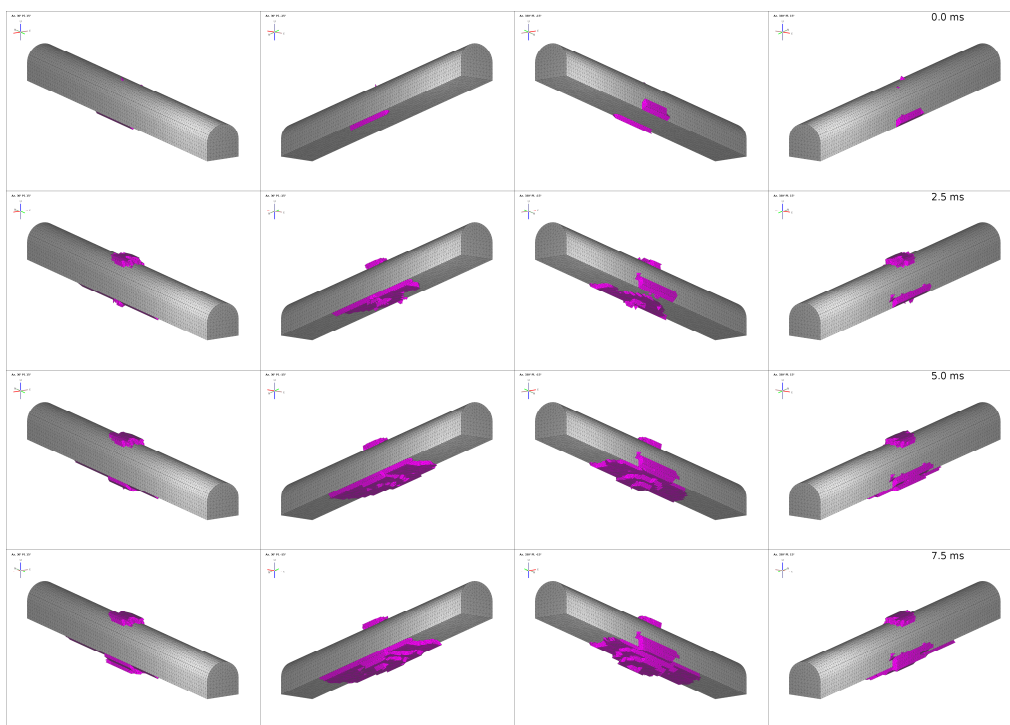

Figure 4 **Progression of failure (purple volume) around the tunnel for Case 1. Each row corresponds to a different point in time (in 2.5 ms increments) and contains views at an azimuth and plunge of 30° and 15°, 30° and -15°, 330° and -15°, and 330° and 15°, respectively. An animated version is available online (Seismology AU 2023a)**

3.2 Case 2: vertical loading, bidirectional failure

For the second case, loading is vertical and material properties are symmetric. As shown in Figure 5, this leads to failure concentrated in both sidewalls that propagates bidirectionally.
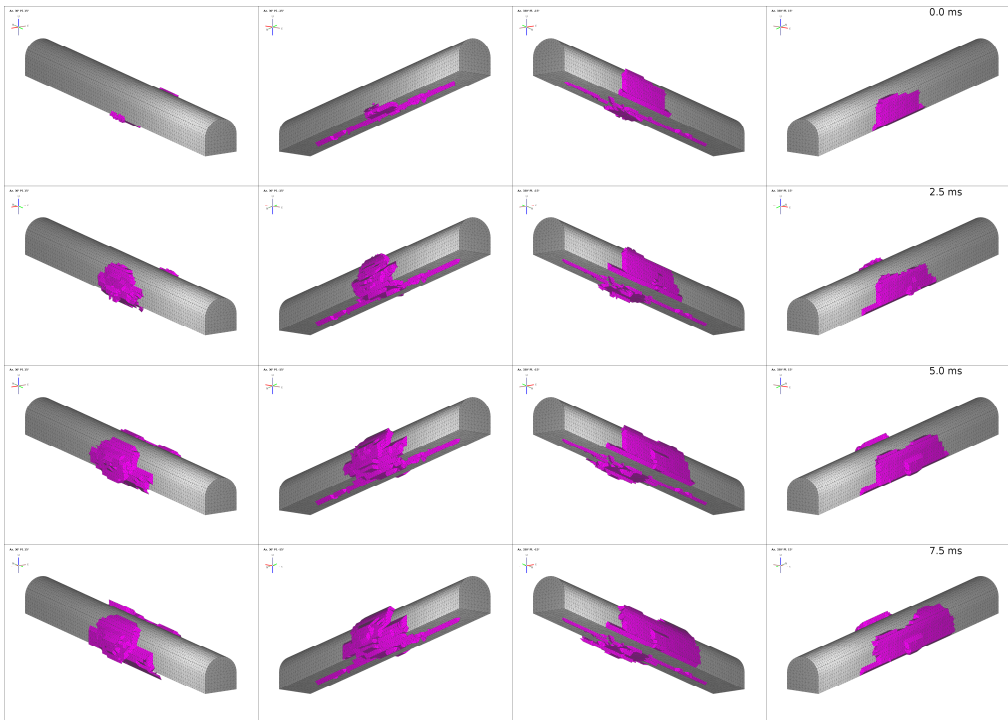
Figure 5   Progression of failure (purple volume) around the tunnel for Case 2. An animated version is available online (Seismology AU 2023b)

3.3   Case 3: horizontal loading, unidirectional failure

For the third case, loading is horizontal and material properties are asymmetric. This leads to failure concentrated in the floor that propagates unidirectionally towards the south, as shown in Figure 6.
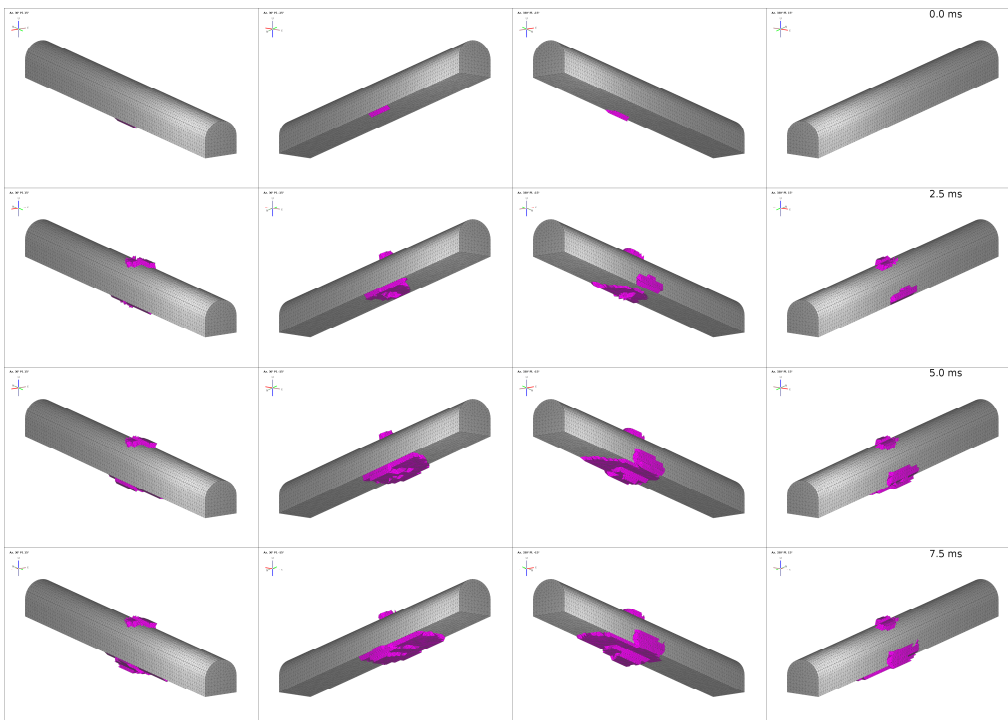

Figure 6   Progression of failure (purple volume) around the tunnel for Case 3. An animated version is available online (Seismology AU 2023c)

3.4 Case 4: vertical loading, unidirectional failure

For the fourth case, loading is vertical and material properties are asymmetric. As shown in Figure 7, this leads to failure concentrated in the sidewalls that propagates (predominantly) unidirectionally towards the south.
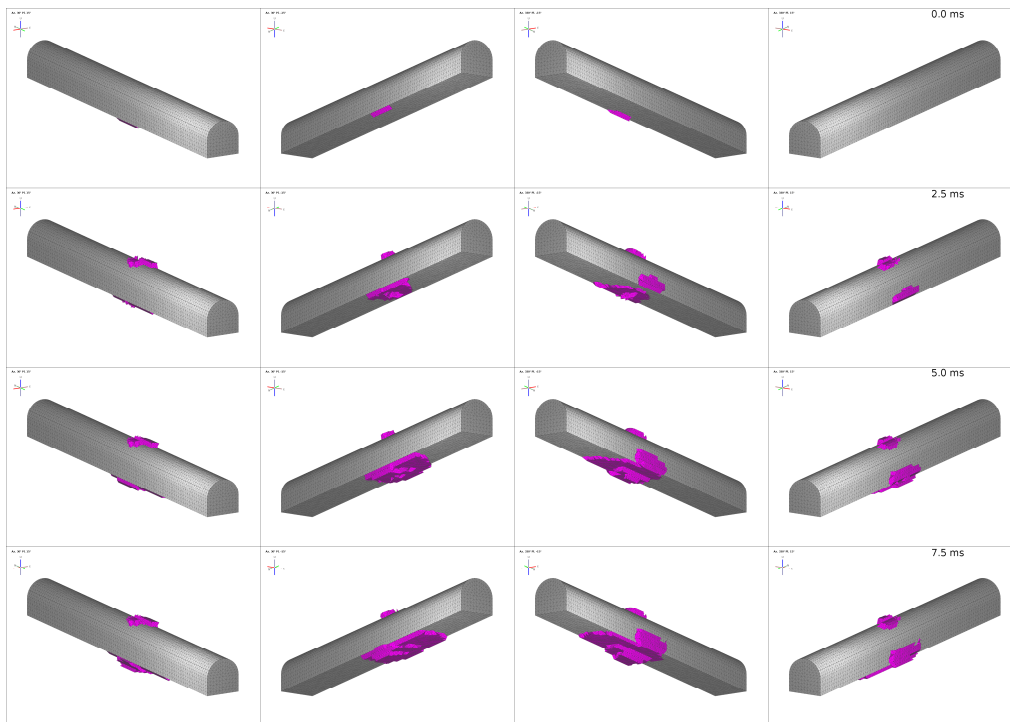

Figure 7 Progression of failure (purple volume) around the tunnel for Case 4. An animated version is available online (Seismology AU 2023d)

4 Failure velocities and durations

4.1 Radial

To analyse the radial evolution of failure, we bin/grid the MPM particles. These bins are 5° angular segments that extend 0.5 m along the tunnel. An example of the geometry of a bin in the western sidewall is shown in Figure 8. Note that while this diagram shows the bin as having finite radial extent, they extend indefinitely in the radial direction in practice.
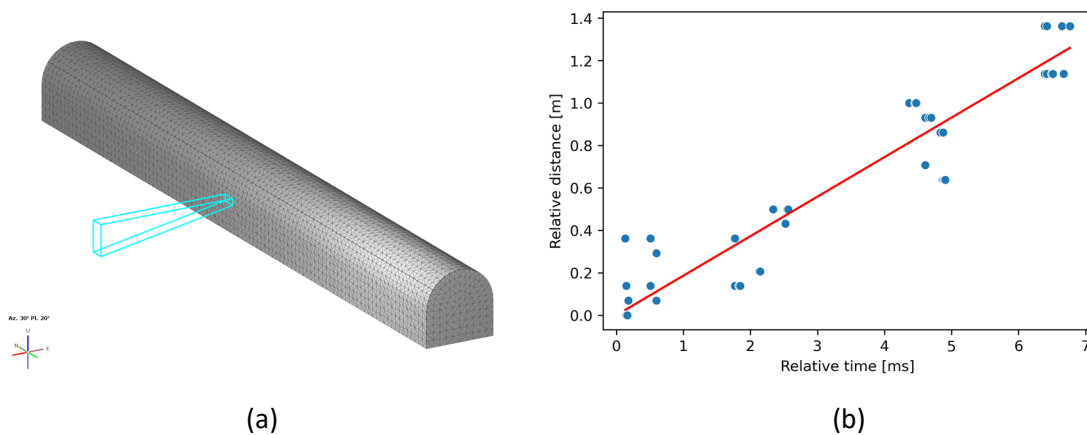

(a)   (b)

Figure 8 (a) Example radial bin geometry; (b) Example of least-squares fit used to determine the radial propagation velocity for a given bin

We calculate three parameters per bin. The first of these is depth of failure increment Δd_f. This is calculated by determining the deepest failed particle (in terms of distance to the tunnel's boundary) before and after the strainburst and calculating the radial distance between them. Contours of this parameter for the four cases outlined in Section 3 are shown in Figure 9a. These plots show an unravelled/unfolded view of the tunnel. When looking north along the tunnel's axis, the angle ϑ gives the anticlockwise angle from the middle of the eastern sidewall. Taking the same convention as Section 2.2, the y coordinate gives the position along the tunnel's axis, with north being positive. As listed in Table 1, the maximum depth of failure increases are approximately 2 m for Cases 1 and 2 and approximately 1.5 m for Cases 3 and 4. Also listed are values of $\Sigma\Delta d_f{}^{max}$, which are the maximum depth of failure increases cumulated across opposing sides of the tunnel.
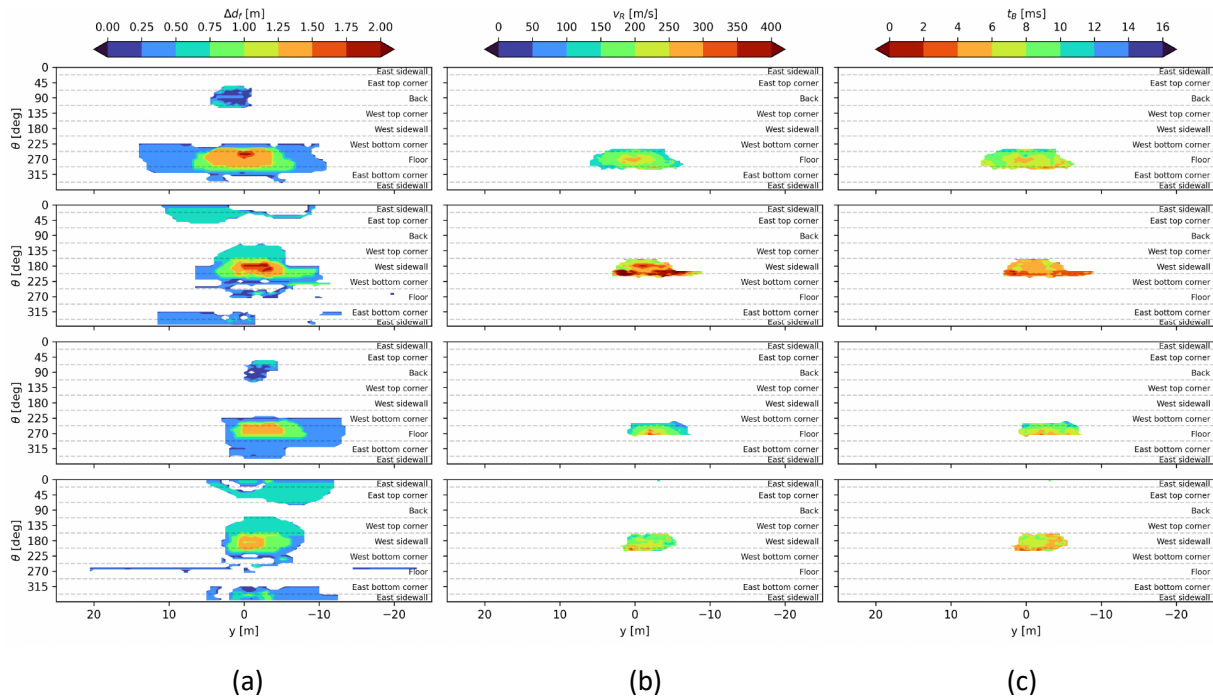

Figure 9   **(a) Contours of depth of failure increase for Case 1; (b) Contours of radial propagation velocity for Case 1; (c) Contours of radial propagation duration for Case 1. The remaining rows shown the same for Cases 2–4**

Table 1   **Maximum depth of failure increment $\Delta d_f{}^{max}$, cumulative (across both sides of the tunnel) maximum depth of failure increment $\Sigma\Delta d_f{}^{max}$, and five-figure summaries (minimum|lower quartile|median|upper quartile|maximum) of radial propagation velocity v_R and duration t_R for the considered cases**

Case	$\Delta d_f{}^{max}$ (m)	$\Sigma\Delta d_f{}^{max}$ (m)	v_R (m/s)	t_R (ms)
1	1.93	2.29	81|136|**165**|196|297	2.03|4.10|**5.07**|6.06|8.64
2	1.93	2.03	90|223|**278**|329|818	1.05|2.90|**3.84**|4.93|6.31
3	1.48	2.03	65|127|**155**|189|344	1.86|4.05|**5.06**|6.08|8.82
4	1.43	1.95	94|149|**185**|220|356	2.42|3.74|**4.30**|5.83|7.77

The second parameter we calculate is radial propagation velocity v_R. This is not to be confused with the velocity of bulking or ejection; instead, it is the velocity at which failure propagates radially. For a given bin, we determine the 'relative' distance and time of failure for every particle that fails during the strainburst. If there are pre-existing failed particles in the bin before the strainburst, then these values will be calculated relative to the nearest such particle. If there is no pre-existing failure, then they are calculated relative to the first particle/s to fail during the strainburst. An example of these values for a randomly selected bin are shown

on the right of Figure 8, with each point corresponding to a particle that failed during the strainburst. To reduce this data to a single velocity for the bin as a whole, we take the slope of a least-squares fit (shown by the red line). Contours of these fitted propagation velocities are shown for each case in Figure 9b. Note that we exclude bins where there is insufficient data (any bin where $\Delta d_f < 0.75$ m or fewer than 20 particles fail during the strainburst) or where the fit is unreliable (normalised root–mean–square error greater than one). A summary of the distribution of values for the remaining bins is listed in Table 1. Here it can be seen that the median radial propagation velocities range from 155 m/s for Case 3 up to 278 m/s for Case 2. Note that this is an order of magnitude less than the propagation velocities for confined shear rupture, which is expected to be comparable to the S-wave velocity (Chounet et al. 2018).

The final parameter we calculate is the radial propagation duration t_R, which is just the ratio $\Delta d_f/v_R$. Contours of this duration are shown in Figure 9c. As listed in Table 1, the median durations range from 3.84 ms for Case 2 up to 5.07 ms for Case 1.

4.2 Axial

We have analysed the evolution of failure along the tunnel's axis in a similar manner to Section 3.1. As shown in Figure 10, the bins used are 5° angular segments that extend 0.5 m radially and span the entire tunnel length.
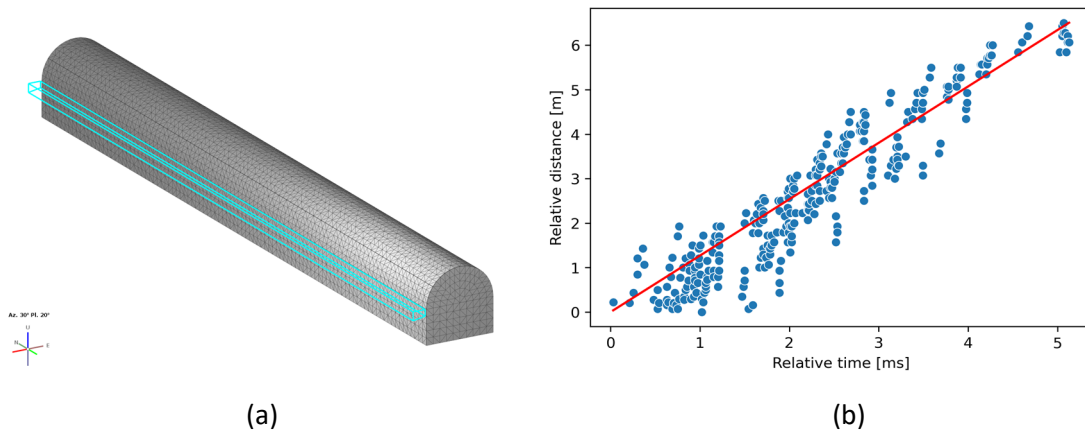

(a)   (b)

Figure 10 (a) Example axial bin geometry; (b) Example of least-squares fit used to determine the axial propagation velocity for a given bin

Again, we calculate three parameters per bin. The first of these is the increase in the span of failure along the tunnel's axis ΔL_A. Contours of this span increase are shown in the left column of Figure 11 for a view looking north along the tunnel.

Following much the same procedure as for the radial bins, we determine the relative distance and time of failure for each particle that fails during the strainburst for a given bin. An example of the resulting values for a randomly selected bin are shown in Figure 10. Again, we reduce this to a single velocity per bin by performing a least-squares fit. Contours of this axial propagation velocity v_A are given in the second column of Figure 11. Here we omit bins following similar criteria as applied in the radial case, the only difference being the substitution of the $\Delta d_f > 0.75$ m criterion for $\Delta L_A > 5$ m. The velocities for the remaining bins are summarised in Table 2, where it can be seen that the median values range from 1,213 m/s for Case 3 up to 1,447 m/s for Case 1. While these are significantly greater than the radial velocities, they are still smaller than would be expected in a case of shear rupture.
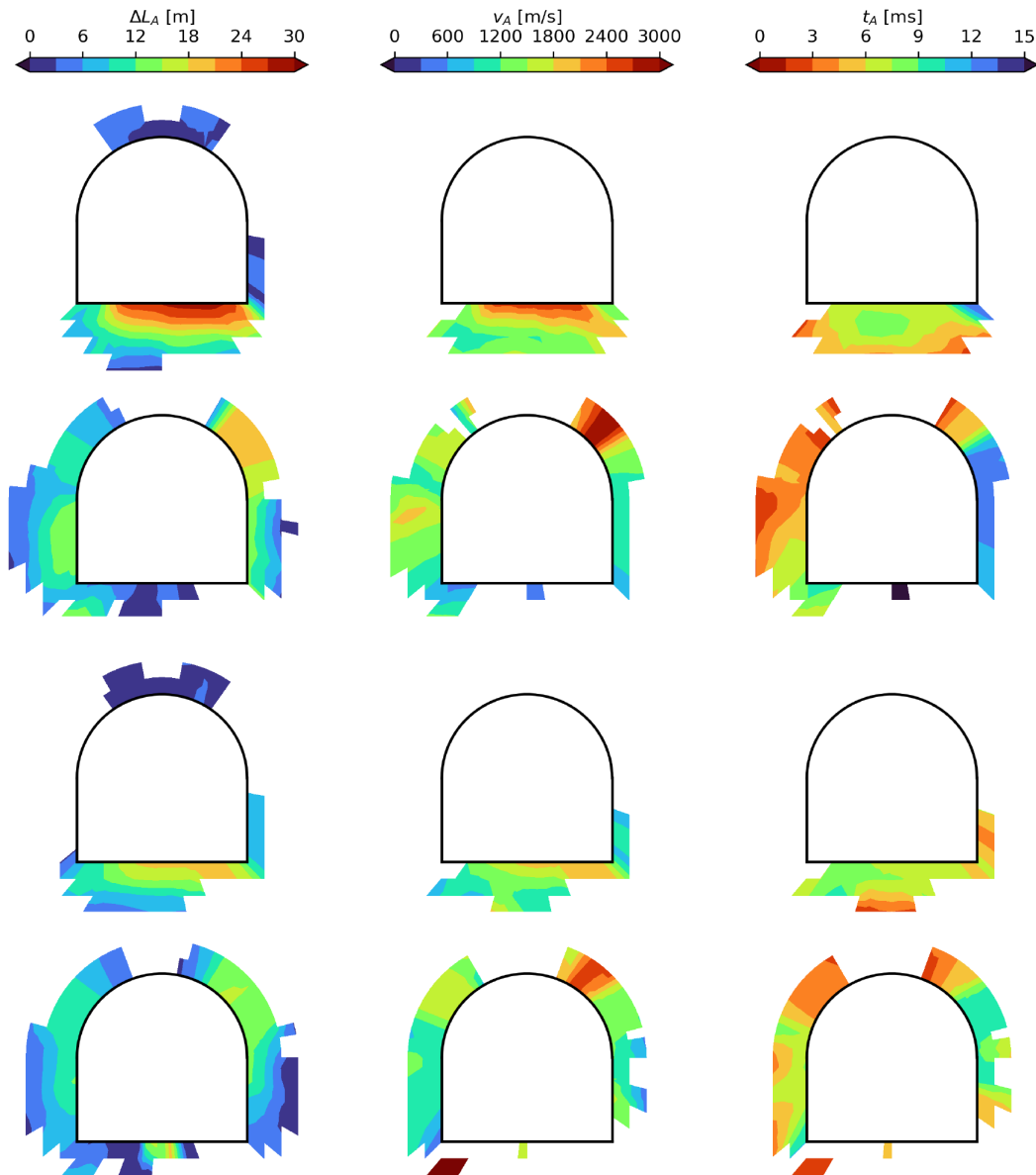
Figure 11   (Top left) Contours of axial failure increase for Case 1 looking north along the tunnel; (Top middle) Contours of axial propagation velocity for Case 1; (Top right) Contours of axial propagation duration for Case 1. The remaining rows shown the same for Cases 2–4

Table 2   Five-figure summaries (minimum|lower quartile|median|upper quartile|maximum) of axial propagation velocity and duration for the considered cases

Case	v_A (m/s)	t_A (ms)
1	797|1,224|**1,447**|2,420|2,676	2.23|4.98|**6.49**|7.12|12.48
2	300|1,103|**1,331**|1,632|3,051	1.56|3.29|**5.74**|11.11|18.33
3	549|926|**1,213**|1,827|2,198	1.48|6.03|**7.04**|7.66|9.86
4	424|1,065|**1,272**|1,625|3,504	2.08|3.98|**5.69**|9.18|10.53

Lastly, we calculate the axial failure duration t_A. Given that failure propagates bidirectionally in some cases, it is not appropriate to calculate this as simply $\Delta L_A/v_A$. Instead, we divide the largest relative distance (as plotted in Figure 10) by the estimated axial propagation velocity. Contours of the resulting values are

shown in the third column of Figure 11. They are also summarised in Table 2, where they range from 5.69 ms for Case 4 up to 7.04 ms for Case 2. These are comparable to the radial durations listed in Table 1.

5 Moment tensors

As discussed by Malovichko (2020), the moment tensor for failure near/involving an excavation can be expressed as the sum

$$M_{ij} = M_{ij}^S + M_{ij}^D,$$

(4)

of a (plastic) strain component M_{ij}^S and displacement component M_{ij}^D. In particular,

$$M_{ij}^S = \iiint_V c_{ijkl}(\boldsymbol{\xi}) \triangle \varepsilon_{kl}(\boldsymbol{\xi}) \, dV(\boldsymbol{\xi}),$$

(5)

where, as shown in Figure 12:

V	=	volume in which rock fails.
$\Delta\varepsilon$	=	difference in plastic strain (after versus before failure).
c_{ijkl}	=	stiffness tensor (elastic, isotropic used here).

and

$$M_{ij}^D = -\iint_\Sigma c_{ijkl}(\boldsymbol{\xi}) \Delta u_k(\boldsymbol{\xi}) n_l(\boldsymbol{\xi}) \, d\Sigma(\boldsymbol{\xi}),$$

(6)

where:

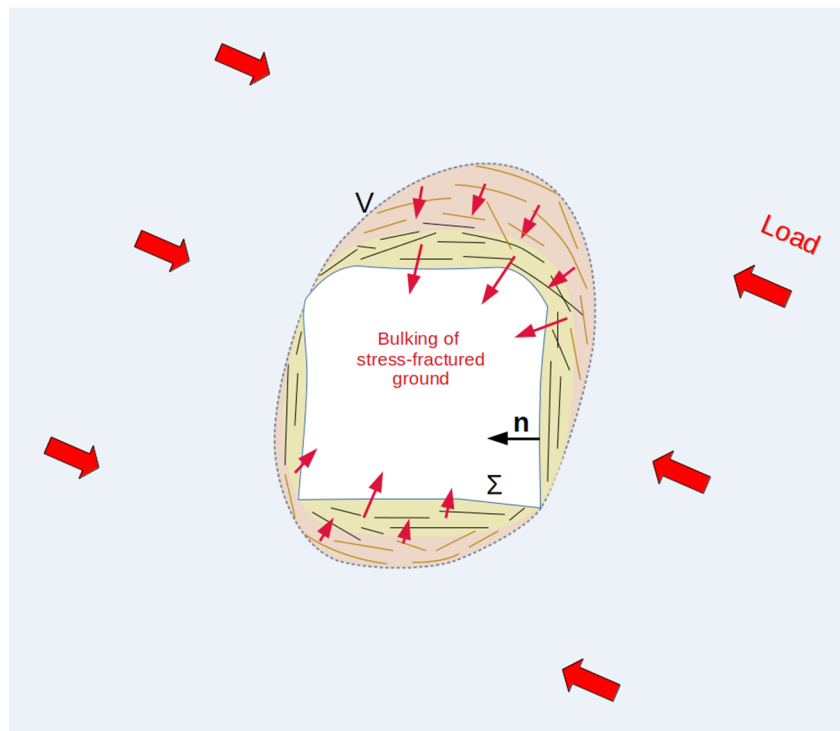|		
Σ	=	tunnel's surface.
Δu	=	difference in displacement of this surface.
N	=	an inward unit normal to Σ.

Figure 12 View looking along a tunnel showing the failed volume of rock *V*, excavation boundary Σ and inward normal n used in Equations 4 and 5

Moment tensors have been calculated using Equation 4 for each of the four cases considered. Corresponding scalar moments and moment magnitudes are listed in Table 3. These magnitudes range from $M_W = 0.73$ for Case 3 up to $M_W = 0.95$ for Case 2. It can be seen that the strain and displacement components combine 'destructively', with each being larger than their combination (that is, $|M| < |M^S| + |M^D|$). This is consistent with the results of two-dimensional modelling conducted by Malovichko & Rigby (2022).

Table 3 Scalar moment |M| (in units of 10^9 N·m) and moment magnitude $M_W = 0.667 \log_{10}|M| - 6.033$ (Hanks & Kanamori 1979) for the cases considered. Each case is separated into a strain component (Equation 5), displacement component (Equation 6), and their combination (Equation 4)

Case	Strain	Displacement	Total
1	40.95|1.04	56.83|1.14	**27.35|0.92**
2	35.52|1.00	54.24|1.12	**29.53|0.95**
3	20.03|0.83	28.44|0.94	**14.07|0.73**
4	26.72|0.92	42.40|1.05	**23.44|0.88**

The counteracting nature of the strain and displacement components is highlighted in the Hudson plot of Figure 13. It can be seen that in all four cases, the strain component is largely explosive, which is a result of dilation. Conversely, the displacement component for each case has strong implosive content. Their combination lies near the closing crack source, which has been proposed as the model for an 'ideal' crush-type source (Malovichko & Rigby 2022).

Figure 13 also shows the orientation of the moment tensors and their components. It can be seen that in each case, the P-axis is approximately aligned with σ_1 (east–west for Cases 1 and 3; vertical for Cases 2 and 4). While the B- and T-axes align with σ_2 and σ_3, respectively, for each case, we do not expect that this will occur in general. The eigenvalues corresponding to the B- and T-axes become degenerate near the closing crack source, making the orientations unstable (and not particularly meaningful).
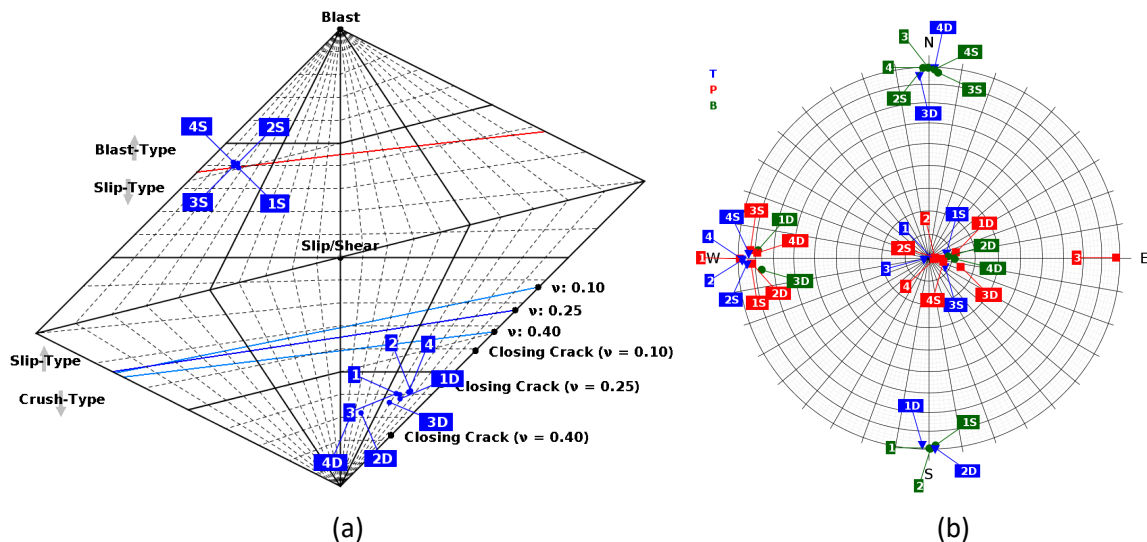

(a)   (b)

Figure 13 (a) Hudson plot showing the source types of the moment tensors and their components ('S' for strain, 'D' for displacement, and no suffix for their sum) for the four cases; (b) Stereonet showing the principal axis orientations for the same moment tensors (T-axis in blue, P-axis in red, and B-axis in green)

6   Conclusion

To better understand the dynamics of strainbursting around an isolated tunnel, dynamic three-dimensional modelling of four different cases has been conducted using the MPM. These cases correspond to variations in loading (vertical or horizontal σ_1) and material parameter distribution (symmetric or asymmetric about the tunnel's centre), which resulted in differing distributions of failure in space (sidewalls or back/floor) and time (bidirectional or unidirectional propagation), respectively.

The results of the four cases have been analysed to estimate the radial and axial propagation velocities and durations for each case. Radial failure propagation velocities and durations ranged from 155 to 278 m/s and 3.84 to 5.07 ms, respectively. Axial failure propagation velocities and durations ranged from 1,213 to 1,447 m/s and 5.69 to 7.04 ms, respectively. It is notable that these velocities, particularly in the case of radial propagation, are significantly lower than is to be expected for shear rupture (Chounet et al. 2018).

Following the methodology of Malovichko (2020), we have also determined moment tensors for each case. In each case, the explosive content contributed by the dilation of failing rock was counteracted by a more significant implosive component corresponding to the convergence of the surrounding rock mass into the excavation. This resulted in moment tensors consistent with those derived by Malovichko & Rigby (2022), having a source type similar to that of a closing crack (that is, crush-type) and a P-axis approximately aligned with the direction of maximum in-plane loading.

There are a several directions in which the work presented in this paper can be logically extended:

- While several cases have been considered, they are far from exhaustive. Future simulations could be conducted that utilise different loading conditions (including loading inclined relative to the tunnel's axis), tunnel profiles (the perfectly flat floor employed here is somewhat unrealistic), material properties/distributions (potentially including anisotropy to better model bulking behaviour), failure seeding methodologies (such as a stress increase or dynamic stress wave), support pressures (this is related to the stiffness of the tunnel material) etc. This would give insight into how variation of these parameters influences the various values/results presented here.

- The mesh used has a resolution of approximately 0.5 m. As a result, the modelled failure only extended a few tetrahedra into the rock mass. Running simulations with a finer mesh would give a more accurate picture of how failure tends to be distributed around and along the tunnel.

- It was noted in Section 1 that strainburst dynamics have implications in terms of the demand placed on ground support. Analysis of this demand is not something that has been conducted directly in this paper, but could be assessed in future work (either using the cases presented here or based on those proposed above).

Acknowledgement

References

Brune, JN 1970, 'Tectonic Stress and the Spectra of Seismic Shear Waves from Earthquakes', *Journal of Geophysical Research*, vol. 75, no. 26, pp. 4997–5009.

Chounet, A, Vallée, M, Causse, M & Courboulex, F 2018, 'Global catalog of earthquake rupture velocities shows anticorrelation between stress drop and rupture velocity', *Tectonophysics*, vol. 733, pp. 148–158.

Diederichs, MS 2007, 'The 2003 Canadian Geotechnical Colloquium: Mechanistic interpretation and practical application of damage and spalling prediction criteria for deep tunnelling', *Canadian Geotechnical Journal*, vol. 44, no.9, pp. 1082–1116.

Gao, F, Kaiser, PK, Stead, D, Eberhardt, E & Elmo, D 2019, 'Numerical simulation of strainbursts using a novel initiation method', *Computers and Geotechnics*, vol. 106, pp. 117–127.

Hajiabdolmajid, V, Kaiser, PK & Martin, CD 2002, 'Modelling brittle failure of rock', *International Journal of Rock Mechanics and Mining Sciences*, vol. 39, no. 6, pp. 731–741.

Hang, S 2015, 'TetGen, a Delaunay-Based quality tetrahedral mesh generator', *ACM Transactions on Mathematical Software*, vol. 41, no. 2, pp. 11.

Hanks, TC & Kanamori, H 1979, 'A moment magnitude scale', *Journal of Geophysical Research: Solid Earth*, vol. 84, no. B5, pp. 2348–2350.

Itasca Consulting Group 2009, 'Theory and background', *FLAC3D: Fast Lagrangian Analysis of Continua in 3 Dimensions*, 4th edn, Itasca Consulting Group, Minneapolis.

Kaiser, PK & Malovichko, DA 2022, 'Energy and displacement demands imposed on rock support by strainburst damage mechanisms', *Proceedings of the Tenth International Symposium on Rockbursts and Seismicity in Mines*, Society for Mining, Metallurgy & Exploration, Englewood.

Malovichko, DA 2020, 'Description of seismic sources in underground mines: theory', *Bulletin of the Seismological Society of America*, vol. 110.

Malovichko, DA 2022, 'Utility of seismic source mechanisms in mining', *Proceedings of the Tenth International Symposium on Rockbursts and Seismicity in Mines*, Society for Mining, Metallurgy & Exploration, Englewood.

Malovichko, DA & Rigby, A 2022, 'Description of seismic sources in underground mines: dynamic stress fracturing around tunnels and strainbursting', *arXiv*, https://doi.org/10.48550/arXiv.2205.07379

Manouchehrian, A & Cai, M 2018, 'Numerical modeling of rockburst near fault zones in deep tunnels', *Tunnelling and Underground Space Technology*, vol. 80, pp. 164–180.

Ryder, JA 1988, 'Excess shear stress in the assessment of geologically hazardous situations', *Journal of the Southern African Institute of Mining and Metallurgy*, vol. 88, no. 1, pp. 27–39.

Seismology AU 2023a, *F-SBM Case 1*, video file, viewed 24 July 2023, https://youtu.be/8umfOWfzJZ4

Seismology AU 2023b, *F-SBM Case 2*, video file, viewed 24 July 2023, https://youtu.be/4riJEGqDzHM

Seismology AU 2023c, *F-SBM Case 3*, video file, viewed 24 July 2023, https://youtu.be/4B6bErb5xsk

Seismology AU 2023d, *F-SBM Case 4*, video file, viewed 24 July 2023, https://youtu.be/YvPISb0YajA

Sørensen, ES, Clausen, J & Damkilde, L 2015, 'Finite element implementation of the Hoek-Brown material model with general strain softening behavior', *International Journal of Rock Mechanics and Mining Sciences*, vol. 78, pp. 163–174.

Wang, B, Vardon, PJ, Hicks, MA & Chen, Z 2016, 'Development of an implicit material point method for geotechnical applications', *Computers and Geotechnics*, vol. 71, pp. 159–167.